RSC Advances

PAPER

View Article Online
View Journal | View Issue

Cite this: *RSC Adv.*, 2022, **12**, 25262

Synthesis of disordered mesoporous silica loaded with ultrasmall-sized CuO nanoparticles based on an alkali-free strategy and its excellent catalytic performance in the reduction of organic dye†

Li Jiaze, Xu Linxu, * Chen Feiyong, Yang Zhigang, Shen Xue, Wang Jin, Xu Sisi and Song Yang *

In this paper, disordered mesoporous silica loaded with ultrasmall-sized and highly dispersed CuO nanoparticles was obtained by an alkali-free strategy. Pre-prepared copper bromoacetate (CuBA) and (3-aminopropyl)triethoxysilane (APTES) were selected as reactants, which can be covalently connected with each other for the formation of functional hybrid precursors. Simultaneously, the protonated amino group with the ability to promote the hydrolysis of silane was generated, avoiding any additional catalyst. The covalent introduction of copper salt by chemical bonding promised the molecular-level dispersion of copper ions, favouring the *in situ* generation of ultrasmall-sized and highly dispersed CuO nanoparticles in the silica matrix. The average diameter of this obtained composited silica material is around 700 nm, and CuO nanoparticles with an average diameter of ~3 nm were uniformly dispersed in the silica matrix. Typically, disordered mesopores were obtained under the thermolysis of organic chains in the hybrid silica matrix; the BET surface area is 77 m^2 g^{-1} and the pore diameter is about 2.5 nm. The catalytic property was investigated and the results show that this obtained CuO@mSiO_2 material has good catalytic performance in the reduction of organic dye with $NaBH_4$ as the reducing agent.

Received 19th August 2022
Accepted 21st August 2022

DOI: 10.1039/d2ra05199k

rsc.li/rsc-advances

Introduction

Chemical catalysis is one of the common methods in the field of wastewater treatment due to its high efficiency and wide applicability.[1–3] For example, the discharge of dyeing wastewater has caused serious environmental problems all over the world because of the stable molecular structure of dyes, which makes it difficult to carry out biochemical treatment.[4] Chemical catalysis can easily damage the molecular structure, turning refractory substances into small molecules. The key for achieving chemical catalysis is the preparation and selection of appropriate catalysts. Metal or metal oxide nanoparticles (mNPs) are considered to be excellent catalysts due to their high activity and selectivity.[5–9] Among them, precious metals such as silver, gold, and platinum have been widely investigated, and quite a number of studies report that such metals have fascinating catalytic performance.[10–13] However, the high price of precious metals also greatly limits the possibility of their practical application. In the case of finding highly efficient catalysts for wastewater treatment, the biggest challenge is to reduce the usage of noble metals or replace them with inexpensive materials. Earth-abundant transition metals such as copper, iron, and cobalt with unfilled d-orbitals always show activation ability, which make them good candidates for replacing these noble metals. Much effort has been devoted to synthesize inexpensive metal nanoparticles (mNPs) with various sizes and morphologies.[14–16] In order to maintain the activity and integrity of mNPs, they are always compounded with carrier materials such as silica, carbon, and polymers. Silica with mesopores is regard as a good substrate due to its high stability, nontoxicity, large specific surface are, and designability.[17] In general, mesoporous silica (mSiO_2) can be synthesized by the hydrolysis and condensation of silicon alkoxides in the presence of acid or alkali catalyst and structure-directing agents.[18–20] However, in the case of constructing mesoporous silica composited with mNPs, the biggest challenge is to construct mesoporous silica loaded with high-content, ultrasmall-sized and highly dispersed active mNPs, on which the property of composited silica materials is strongly dependent.[21–24] For instance, the coating and impregnation methods are two common methods for the preparation of mNPs/mSiO_2 nanocomposites.[25,26] However, the size and dispersion of mNPs are difficult to control in the coating method because the pre-synthesized mNPs can no longer change, while in the impregnation method, the content of mNPs is unsatisfactory, which may severely limit the application of such materials.

Institute of Resources and Environment Innovation, Shang Dong Jianzhu University, Jinan, 250101, People's Republic of China. E-mail: xulinxu20@sdjzu.edu.cn; songyang20@sdjzu.edu.cn

† Electronic supplementary information (ESI) available: FT-IR; XPS; SEM and TEM data and so on. See https://doi.org/10.1039/d2ra05199k

If the mNPs can be generated *in situ* in mesoporous silica, it may favour the formation of mesoporous silica loaded with high-content and highly dispersed mNPs. The key point for implementing this strategy is the introduction of the metal ion precursor (such as metal salts) into the silica matrix. For the sake of non-destructively introducing metal salts into the silica matrix, neutral or near-neutral conditions are necessary. Herein, we present an alkali-free strategy to prepare the CuO@mSiO$_2$ nanocomposite. CuO was chosen as the functional nanoparticle material due to its extensive application. For example, Zhang *et al.* reported novel hollow CuO microspheres with open nanoholes composed of numerous small CuO crystalline grains, which have excellent photocatalytic activity in the degradation of methyl orange;[27] Wang *et al.* fabricated the lithiophilic CuO-based nanocomposite that can effectively inhibit the growth of Li dendrites and volume expansion during cycling;[28] Nandi *et al.* reported a composited CuO/mSiO$_2$ structure that has good catalytic performance in the syntheses of symmetrical diselenides.[29] Organic copper salt was connected on silicon alkoxides by covalent bonding, leading to the formation of a multifunctional precursor containing copper ions and silanol groups. Most importantly, protonated amino groups that can promote the hydrolysis and condensation of silanol groups to form Si–O–Si networks were generated synchronously,[30] avoiding any additional acid–base catalyst as well as ensuring that the copper ions can be well protected. Covalent introduction can afford a molecular-level dispersion of copper ions; after thermal treatment, CuO NPs can be generated *in situ*, and the disordered mesopores can be formed by the pyrolysis of cetyltrimethylammonium bromide and the organic carbon chains.

Experimental

Materials

(3-Aminopropyl)triethoxysilane (APTES, ≥99%), bromoacetic acid (HBA, ≥99%), cetyltrimethylammonium bromide (CTAB) and polyvinylpyrrolidone (PVP, M_w = 58 000) were purchased from Macklin Corporation (Shanghai, China). Basic cupric carbonate ($Cu_2(OH)_2CO_3$, 99.9%) and absolute ethanol (EtOH, ≥99.7%) were purchased from Sinopharm Chemical Reagent Co., Ltd (Shanghai, China). Water used in the experiments was deionized with a resistivity of 18.2 MΩ cm^{-1}. All the reagents were used as obtained without further purification.

Preparation of copper salt

Copper salt was obtained using HBA and $Cu_2(OH)_2CO_3$ as reagents. Typically, HBA (0.1 mol, 13.89 g) and $Cu_2(OH)_2CO_3$ (0.05 mol, 11.05 g) were mixed in 100 mL deionized water under stirring at 60 °C; after reacting for 24 h, the mixture was filtered and the filtered liquor was subjected to vacuum-rotary evaporation at 50 °C to remove the water and unreacted HBA. Finally, the blue powder was collected (named as CuBA).

Preparation of the CuO@mSiO$_2$ nanocomposite

PVP and CTAB were chosen as structure-directing agents. Typically, PVP (0.5 g) and CTAB (0.25 g) were dissolved in 18 mL absolute ethanol, and APTES (2.4 mL, 10 mmol) was then rapidly injected into the ethanol solution under vigorous stirring. After 2 min, the as-obtained CuBA powder (0.447 g, 0.025 mmol) was dissolved in 18 mL absolute ethanol and 1 mL deionized water, and then added to the ethanol solution containing PVP, CTAB and APTES. The whole process was subjected to magnetic stirring at 60 °C for 4 h. After that, the resultant solution was kept undisturbed at room temperature (20 °C) overnight. The deposits were collected after centrifugation, washed with ethanol several times and transferred to an oven at 60 °C to dry (named as CuBA@SiO$_2$). Finally, the deposits were calcined at 600 °C for 2 h to obtain the CuO@mSiO$_2$ nanocomposite.

Catalytic performance testing

The catalytic property of the CuO@mSiO$_2$ composite was tested by studying the change in the intensity at the maximum absorbance wavelength (λ_{max}) of methylene blue (MB) dye. Typically, the CuO@mSiO$_2$ composite (2 mg) was homogeneously dispersed in a 2.5 mL MB dye solution (0.01 mg mL^{-1}), followed by the rapid injection of 0.5 mL $NaBH_4$ solution (0.5 mg mL^{-1}). In the recycling study, the catalysts were separated from the solution by centrifugation after the reduction reaction was completely finished. After washing with water twice, the catalyst was used in the next reaction run. The procedure was repeated 6 times.

Characterization

Fourier-transform infrared (FT-IR) spectra were recorded using a KBr carrier containing the powder sample using an ENSOR spectrometer. A JSM-7610FPlus scanning electron microscope (SEM) with a primary electron energy of 15 kV was employed to examine the surface morphologies of the products. TEM images were obtained using an FEI Tecnai G2F30 transmission electron microscope with an accelerating voltage of 200 kV. X-ray diffraction (XRD) data were collected with a Rigaku D/Max-2500 X-ray diffractometer using a Cu target radiation source. Ultraviolet-visible (UV-vis) spectra were acquired at room temperature using a SHIMADZU 3100 UV-vis-near-IR spectrophotometer. X-ray photoelectron spectra (XPS) were collected using a VG ESCALAB MKII with Al Kα excitation (1361 eV). Binding energy calibration was based on the C 1s spectrum at 284.6 eV. Inductively coupled plasma (ICP) atomic emission spectroscopy measurements were performed on an Optima 7000 DV.

Results and discussion

Scheme 1 shows the synthetic pathway for the preparation of the CuO@mSiO$_2$ nanocomposite. A nucleophilic substitution reaction took place when APTES was mixed with CuBA because there is an electron-rich amino group on APTES and an electron-deficient α-C on the CuBA molecule. This nucleophilic substitution reaction not only resulted in the covalent linkage of copper ions and silanol groups but also simultaneously generated the protonated amino group; thus, the sol–gel process can

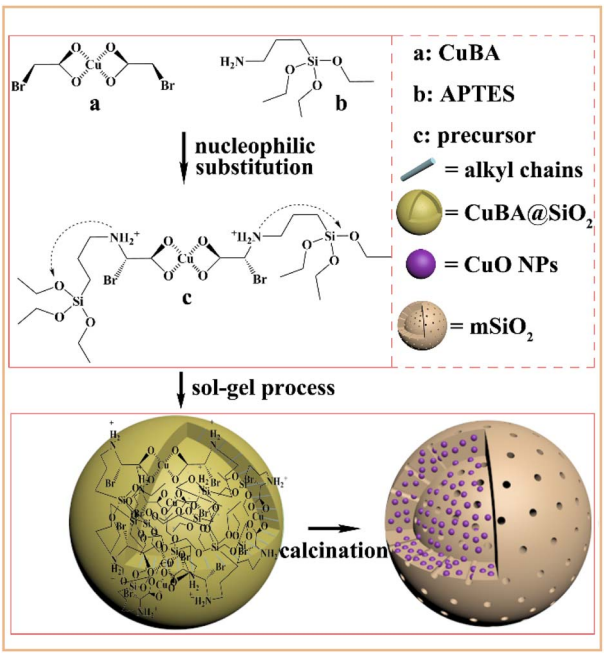

Scheme 1 Synthetic pathway for the preparation of the CuO@mSiO$_2$ nanocomposite.

occur spontaneously under alkali-free conditions, allowing the intact introduction of copper salts. Moreover, the covalent bond between copper salts and APTES can make it possible to achieve the molecular-level dispersion of copper ions in the silica matrix, which is key for the formation of ultrasmall and highly dispersed CuO nanoparticles. Finally, copper salts were transferred into CuO nanoparticles *in situ* under thermal treatment; meanwhile, the alkyl chains were decomposed to form the mesopores.

The pre-synthesized CuBA was characterized by FT-IR. The strong peaks shown at 1613, 1407, 707 and 570 cm^{-1} (Fig. S1, ESI†) can be assigned to the antisymmetric stretching vibration, symmetric stretching vibration and deformation vibration of the carboxylate groups and the stretching vibration of the C–Br groups, respectively, indicating that CuBA was successfully obtained. Fig. 1 shows the FT-IR spectrum of the hybrid CuBA@SiO$_2$ materials, wherein the presence of all the characteristic absorption peaks of CuBA demonstrated that the organic copper salt was well-protected during the sol–gel process and embedded in Si–O–Si networks. A strong peak at 1134 cm^{-1} can be clearly observed, which can be assigned to the secondary amine group, indicating that the nucleophilic substitution reaction indeed occurred. The peaks at 1094 and 924 cm^{-1} can be ascribed to the antisymmetric and symmetric stretching vibrations of the organic Si–O–Si networks, respectively. The three adjacent peaks located at 788, 750 and 698 cm^{-1} are typical of Si–C stretching, confirming that the organic chains are covalently bound on the Si–O–Si networks. Finally, the hybrid CuBA@SiO$_2$ material was converted to the CuO@mSiO$_2$ nanocomposite by thermal treatment. The peaks located at 1100 and 802 cm^{-1} (Fig. S2, ESI†) are ascribed to the antisymmetric stretching vibration and symmetric stretching

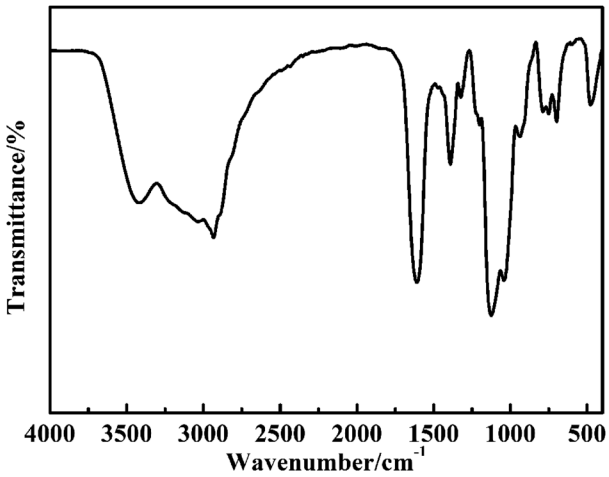

Fig. 1 FT-IR spectrum of the CuBA@SiO$_2$ material.

vibration of amorphous Si–O–Si, respectively, which can be explained by the fact that organosilicon transformed into amorphous silica materials.

The microstructure of the pre-obtained CuBA@SiO$_2$ material was analysed by SEM and TEM. Fig. 2(A) shows that CuBA@SiO$_2$ has a spherical morphology with an average diameter of ~900 nm. Fig. 2(B) shows a typical TEM image of the CuBA@SiO$_2$ nanocomposite; a compact and homogeneous interior structure can be observed, showing that the organic copper salt was dispersed in the whole silica matrix, which is promising for generating a high content of CuO NPs. Fig. 2(C) shows the EDS spectra of the as-obtained material with information on the elements of C, O, Cu, Br and Si, which also provides the evidence that CuBA has been well-protected. Further analysis of the spatial distribution of elements has been performed by EDX elemental mapping and line-scanning; the results are shown in Fig. 2(D–K), which illustrate that all the elements are homogeneously dispersed in the silica matrix, allowing the preparation of silica material loaded with highly dispersed CuO nanoparticles.

The CuO@mSiO$_2$ nanocomposite was obtained by the pyrolysis of the hybrid CuBA@SiO$_2$ material. The

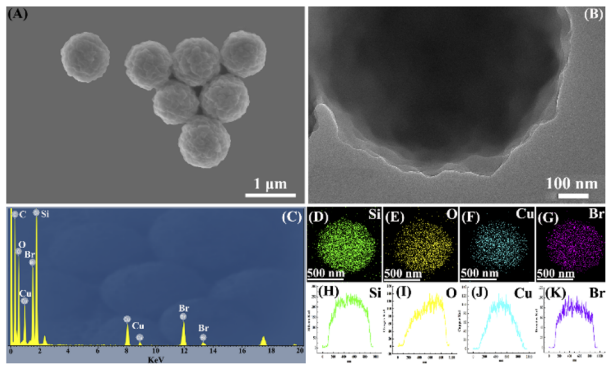

Fig. 2 SEM image (A), TEM image (B), EDS spectrum (C), EDX elemental mapping (D–G) and EDX line-scan images (H–K) of the CuBA@SiO$_2$ material.

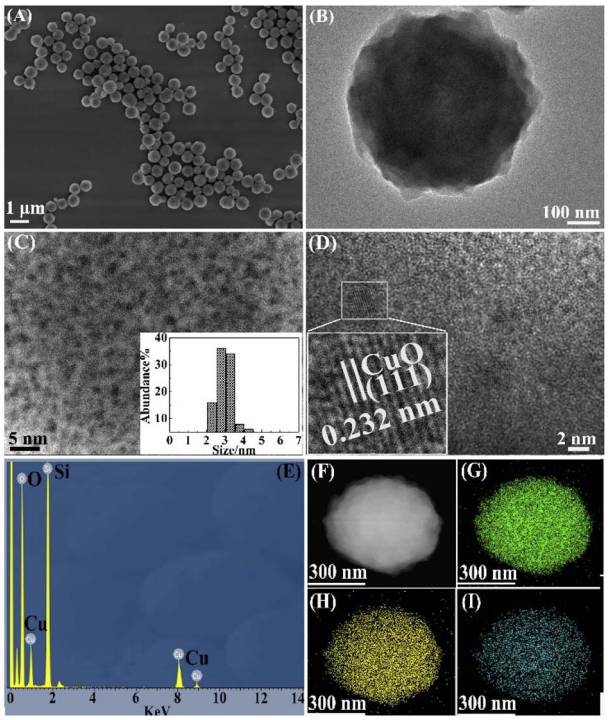

Fig. 3 SEM image (A), TEM image (B), magnified TEM image (C), HRTEM image (D), EDS spectrum (E), HADDF image (F) and EDX elemental mapping (G–I) of the CuO@mSiO$_2$ material.

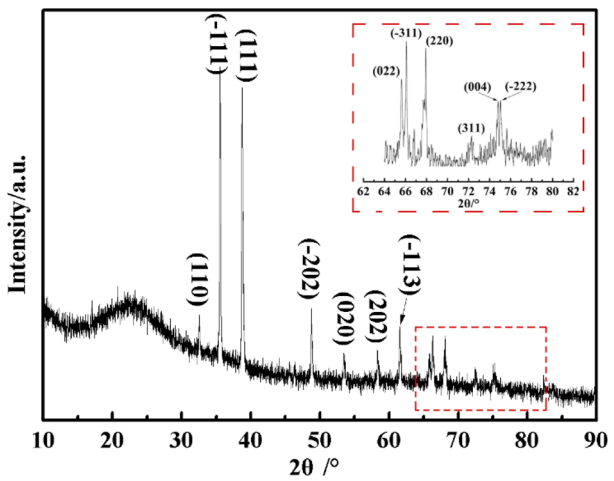

Fig. 4 XRD pattern of CuO@mSiO$_2$ material.

microstructure of the CuO@mSiO$_2$ nanocomposite is shown in Fig. 3. From Fig. 3(A), we can see that the average diameter of CuO@mSiO$_2$ is reduced to ~700 nm, mainly because of the high proportion of organic ingredients in the organic–inorganic hybrid CuBA@SiO$_2$ material. However, the spherical morphology shows no significant change in the process of calcination, which reveals the good mechanical property and stability of the hybrid silica material. The typical TEM image shown in Fig. 3(B) presents a uniform interior structure. The magnified TEM image shown in Fig. 3(C) gives the additional information that CuO NPs with an average diameter of ~3 nm (inset in Fig. 3(C) shows the statistics of the size distribution) are uniformly dispersed in the whole silica matrix. For more evidence of the generation of CuO NPs, Fig. 3(D) shows the high-resolution TEM image with an enlarged selected part, which presented a clear crystalline lattice with an interplanar spacing of 0.232 nm, corresponding to the (111) lattice of CuO crystals (JCPDS no. 80-1916). The EDS spectrum (Fig. 3(E)) presents the remaining elements of O, Si and Cu after thermal treatment. Fig. 3(G–I) present the EDX elemental mapping images of the CuO@mSiO$_2$ material, giving further information on the well-dispersed CuO NPs.

Further information about the obtained CuO@mSiO$_2$ material was acquired by XRD. As shown in Fig. 4, a dispersive characteristic peak is presented at $2\theta = 22.8°$, which can be assigned to the amorphous silica matrix. The diffraction peaks at $2\theta = 32.5°$, $35.5°$, $38.6°$, $48.6°$, $53.5°$, $58.3°$, $61.4°$, $65.8°$, $66°$, $68°$, $72.3°$, $74.9°$ and $75.1°$ (magnified inset image) can be indexed to the (110), (−111), (111), (−202), (020), (202), (−113), (022), (−311), (220), (311), (004) and (−222) planes of the CuO crystal, respectively, with the cell parameters of $a = 4.692$, $b = 3.428$, $c = 5.317$ and $\beta = 99.546$ (JCPDS no. 80-1916). The result of XRD illustrates that CuO NPs with high crystallinity were generated *in situ* in the silica matrix, which also agrees with the TEM data.

Fig. 5 shows the N_2 adsorption–desorption isotherm of the as-obtained CuO@mSiO$_2$ nanocomposite. A typical type IV isotherm with a type H4 hysteresis loop, which indicates a composited silica material with disordered vermiculate pores, was obtained.[31] The BET surface area is 77 m^2 g^{-1} and the pore diameter is about 2.5 nm. CuBA was covalently linked with APTES, and there are several alkyl chains distributed in the silica matrix when the sol–gel process occurred. Moreover, the use of CTAB provides more organic placeholders. During the thermolysis of the hybrid CuBA@SiO$_2$ material, the alkyl chains were carbonized *via* chemical decomposition and were confined as vesicles in the silica matrix, which were converted into mesopores.

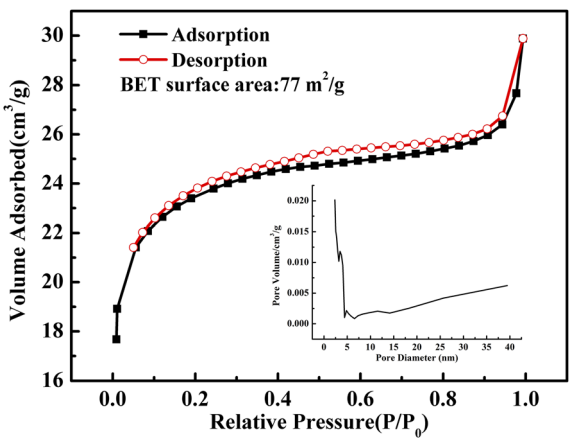

Fig. 5 N_2 adsorption–desorption isotherm of the as-obtained CuO@mSiO$_2$ material; the inset shows the pore diameter distribution of the CuO@mSiO$_2$ material.

In this paper, the catalytic activity of the obtained CuO@mSiO$_2$ nanocomposite was estimated by employing the reduction of MB dye with NaBH$_4$ as a reductant. Fig. 6(A) shows the UV-vis spectra of MB dye in the presence and absence of CuO@mSiO$_2$. Curve (*a*) is the spectrum of the original MB dye with λ_{max} at 664 nm. Curve (*b*) shows the spectrum of the mixture of MB dye and NaBH$_4$ reductant after 12 h, showing that the intensity at λ_{max} decayed and the value was found to be 32.8%. Curve (*c*) is the spectrum of the mixture of the MB dye and the NaBH$_4$ reductant in the presence of CuO@mSiO$_2$; the intensity at λ_{max} almost decreased to zero within 1 min, demonstrating the excellent catalytic activity in the reduction of organic dye.

In order to monitor the reaction rate of the MB dye solution with NaBH$_4$ and the CuO@mSiO$_2$ material, we had to reduce the amount of CuO@mSiO$_2$ to 0.1 mg. Fig. 6(B) shows the UV-vis spectra of the MB dye at different times in the presence of 0.1 mg CuO@mSiO$_2$ nanocatalyst. The rate constant K was determined using a linear plot of $\ln(C_t/C_0)$ and reaction time t (C_t and C_0 are the MB dye concentrations at time t and 0, respectively, measured from the relative intensity of the respective absorbance A_t and A_0). The constant K was calculated from the equation $\ln(C_t/C_0) = Kt$, and the slope of the linear fit result was 0.134 min^{-1}. To further compare our result with the reported values, the catalytic activity K' was calculated ($K' = K/M_{CuO}$, where M_{CuO} is the total mass of the CuO NPs measured by ICP measurements, and the value is 12.8%). The K' of the obtained CuO@mSiO$_2$ nanocomposite is 174.4 s^{-1} g^{-1}, which is higher than that of some reported noble metal catalysts[32–37] (for detailed comparative information, see Table S1, ESI†).

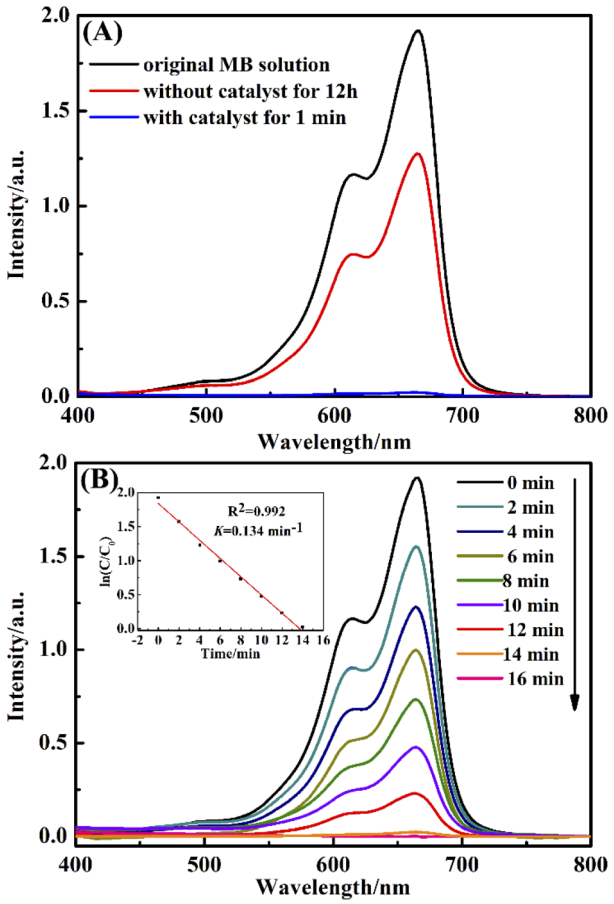

Fig. 6 (A) UV-vis spectra of the original MB solution; the mixture of MB and NaBH$_4$ solution after 12 h; and the mixture of MB and NaBH$_4$ solution after 1 min in the presence of 2 mg CuO@mSiO$_2$ nanocomposite. (B) UV-vis spectra of MB and NaBH$_4$ in the presence of 0.1 mg CuO@mSiO$_2$ nanocomposite at different times; the inset shows the rate constant (*k*) estimated using the slopes of the straight lines of $\ln(C_t/C_0)$ *vs.* reaction time.

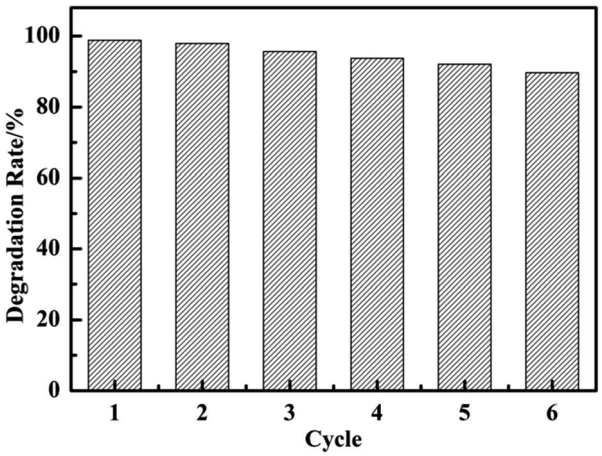

Fig. 7 The degradation rate of each cycle of MB solution in the presence of 2 mg CuO@mSiO$_2$ catalyst in 1 min.

The reusability of CuO@mSiO$_2$ was also tested. The intensity at λ_{max} of the MB dye was immediately measured after the reaction with 2 mg catalyst for 1 min in each cycle. As shown in Fig. 7, the degradation of MB dye could still reach up to 90% even after 6 cycles. The main reason is because the loss of the catalyst could not be avoided during the processes of collection and washing, which inevitably affects the catalytic activity.

Conclusions

In conclusion, we present an alkali-free strategy for preparing spherical silica with disordered mesopore-loaded ultrasmall-sized, highly dispersed and high-content CuO NPs. The obtained nanocomposite has excellent catalytic activity in the reduction of organic dye. Compared with the traditional pathway that requires extreme pH conditions and a multistep process for constructing mesoporous silica loaded with metal or metal oxide nanoparticles, this route is facile and efficient. However, more efforts must be devoted to the synthesis of highly ordered mesoporous silica loaded with high-content and highly dispersed functional nanoparticles under this presented route, which may provide the possibility for the practical application of mesoporous silicon materials.

Conflicts of interest

There are no conflicts to declare.

Acknowledgements

We gratefully acknowledge the financial support from the Doctoral Research Foundation of Shandong Jianzhu University (No. X21074Z).

Notes and references

1 P. Kolosov and V. Yargeau, Impact of catalyst load, chemical oxygen demand and nitrite on disinfection and removal of contaminants during catalytic ozonation of wastewater, *Sci. Total Environ.*, 2019, **651**, 2139–2147.

2 Z. P. Li, F. Liu, Y. Ding, F. Wang, H. You and C. Jin, Preparation and properties of Cu–Ni bimetallic oxide catalyst supported on activated carbon for microwave assisted catalytic wet hydrogen peroxide oxidation for biologically pretreated coal chemical industry wastewater treatment, *Chemosphere*, 2019, **214**, 17–24.

3 J. L. Wang and R. Zhuan, Degradation of antibiotics by advanced oxidation processes: an overview, *Sci. Total Environ.*, 2020, **701**, 135023.

4 Q. Y. Yue, B. Y. Gao, Y. Wang, H. Zhang, X. Sun, S. G. Wang and R. R. Gu, Synthesis of polyamine flocculants and their potential use in treating dye wastewater, *J. Hazard. Mater.*, 2008, **152**, 221–227.

5 P. Falcaro, R. Ricco, A. Yazdi, I. Imaz, S. Furukawa, D. Maspoch, R. Ameloot, J. D. Evans and C. J. Doonan, Application of metal and metal oxide nanoparticles@MOFs, *Coord. Chem. Rev.*, 2016, **307**, 237–254.

6 R. Sankar, P. K. S. M. Rahman, K. Varunkumar, C. Anusha, A. Kalaiarasi, K. S. Shivashangari and V. Ravikumar, Facile synthesis of Curcuma longa tuber powder engineered metal nanoparticles for bioimaging applications, *J. Mol. Struct.*, 2017, **1129**, 8–16.

7 M. Hu, Y. C. Yan, K. Huang, A. Khan, X. D. Qiu, D. K. Xu, H. Zhang and X. G. Yu, Performance improvement of graphene/silicon photodetectors using high work function metal nanoparticles with plasma effect, *Adv. Opt. Mater.*, 2018, **6**, 1701243.

8 L. X. Xu, F. Cui, J. J. Zhang, Y. J. Hao, Y. Wang and T. Y. Cui, Autocatalytic synthesis of multifunctional precursors for fabricating silica microspheres with well-dispersed Ag and Co_3O_4 nanoparticles, *Nanoscale*, 2017, **9**, 899–906.

9 B. Giacomo and C. Paola, Metal complexes and nanoparticles for energy upconversion, *Dalton Trans.*, 2018, **47**, 8507–8508.

10 V. Vaiano, M. Matarangolo, J. J. Murcia, H. Rojas, J. A. Navio and M. C. Hidalgo, Enhanced photocatalytic removal of phenol from aqueous solutions using ZnO modified with Ag, *Appl. Catal., B*, 2018, **225**, 197–206.

11 T. Liu, Y. H. Sun, B. Jiang, W. Guo, W. Qin, Y. M. Xie, B. Zhao, L. Zhao, Z. Q. Liang and L. Jiang, Pd nanoparticle-decorated 3D-printed hierarchically porous TiO_2 scaffolds for the efficient reduction of a highly concentrated 4-nitrophenol solution, *ACS Appl. Mater. Interfaces*, 2020, **12**, 28100–28109.

12 H. T. Wang, Z. X. Dong and C. Z. Na, Hierarchical carbon nanotube membrane-supported gold nanoparticles for rapid catalytic reduction of p-Nitrophenol, *ACS Sustainable Chem. Eng.*, 2013, **1**, 746–752.

13 V. M. Daskalaki, M. Antoniadou, G. L. Puma, D. I. Kondarides and P. Lianos, Solar light-responsive Pt/CdS/TiO_2 photocatalysts for hydrogen production and simultaneous degradation of inorganic or organic sacrificial agents in wastewater, *Environ. Sci. Technol.*, 2010, **44**, 7200–7205.

14 J. Zhu, L. S. Hu, P. X. Zhao, L. Y. S. Lee and K. Y. Wong, Recent advances in electrocatalytic hydrogen evolution using nanoparticles, *Chem. Rev.*, 2020, **120**, 851–918.

15 P. J. Duan, T. F. Ma, Y. Yue, Y. W. Li, X. Zhang, Y. A. Shang, B. Y. Gao, Q. Z. Zhang, Q. Y. Yue and X. Xu, Fe/Mn nanoparticles encapsulated in nitrogen-doped carbon nanotubes as a peroxymonosulfate activator for acetamiprid degradation, *Environ. Sci.: Nano*, 2019, **6**, 1799–1811.

16 G. L. De Gregorio, T. Burdyny, A. Loiudice, P. Iyengar, W. A. Smith and R. Buonsanti, Facet-dependent selectivity of Cu catalysts in electrochemical CO_2 reduction at commercially viable current densities, *ACS Catal.*, 2020, **10**, 4854–4862.

17 G. Peerzada, P. Jeelani, R. Mulay and C. R. Venkat, Multifaceted application of silica nanoparticles: a review, *Silicon*, 2020, **12**, 1337–1354.

18 Y. D. Han, M. Y. Han and W. S. Yang, Sol–gel construction of mesoporous silica nanomicrostructures, *Chem. J. Chin. Univ.*, 2021, **42**, 965–977.

19 Z. Y. Xie, L. Bai, S. W. Huang, C. Zhu, Y. J. Zhao and Z. Z. Gu, New strategy for surface functionalization of periodic mesoporous silica based on meso-$HSiO_{1.5}$, *J. Am. Chem. Soc.*, 2014, **136**, 1178–1181.

20 A. Marjani, R. Soltani, M. Pishnamazi, M. Rezakazemi and S. Shirazian, Functionalized pollen-like mesoporous silica, *Microporous Mesoporous Mater.*, 2021, **310**, 110531.

21 L. X. Xu, F. Cui, J. J. Zhang, X. Zhang, Y. Wang and T. Y. Cui, A general autocatalytic route toward silica nanospheres with ultrasmall sized and well-dispersed metal oxide nanoparticles, *Nanoscale*, 2018, **10**, 9460–9465.

22 H. B. Guo, S. Yi, K. Feng, Y. Q. Xia, X. W. Qu, F. Wan, L. Chen and C. L. Zhang, In situ formation of metal organic framework onto gold nanorods/mesoporous silica with functional integration for targeted theranostics, *Chem. Eng. J.*, 2021, **403**, 126432.

23 C. C. Lin, Y. J. Guo and J. Vela, Microstructure effects on the water oxidation activity of Co_3O_4/porous silica nanocomposites, *ACS Catal.*, 2015, **5**, 1037.

24 Z. X. Li, M. L. Hu, J. H. Liu, W. W. Wang, Y. J. Li, W. B. Fan, Y. X. Gong, J. S. Yao, P. Wang, M. He and Y. L. Li, Mesoporous silica stabilized MOF nanoreactor for highly selective semi-hydrogenation of phenylacetylene via synergistic effect of Pd and Ru single site, *Nano Res.*, 2022, **15**, 1983–1992.

25 R. K. Kankala, H. G. Zhang, C. G. Liu, K. R. Kanubaddi, C. H. Lee, S. B. Wang, W. G. Cui, H. A. Santos, K. L. Lin

and A. Z. Chen, Metal species-encapsulated mesoporous silica nanoparticles: current advancements and latest breakthroughs, *Adv. Funct. Mater.*, 2019, **29**, 1902652.

26 S. M. Zienkiewicz, M. A. Derylo and S. Pikus, Bimetallic systems of mesoporous ordered silica supports and noble metals nanoparticles, *Microporous Mesoporous Mater.*, 2016, **227**, 228–241.

27 S. B. Wang, X. Q. Wang, H. L. Zhang and W. B. Zhang, Hollow CuO microspheres with open nanoholes: fabrication and photocatalytic properties, *J. Alloys Compd.*, 2016, **685**, 22–27.

28 K. Huang, Z. Li, Q. J. Xu, H. M. Liu, H. X. Li and Y. G. Wang, Lithiophilic CuO nanoflowers on Ti-Mesh inducing lithium lateral plating enabling stable lithium-metal anodes with ultrahigh rates and ultralong cycle Life, *Adv. Energy Mater.*, 2019, **9**, 1900853.

29 D. R. Trisha, A. Chatterjee, H. U. Majee, M. David and N. Mahasweta, In situ synthesis of CuO nanoparticles over functionalized mesoporous silica and their application in catalytic syntheses of symmetrical diselenides, *Dalton Trans.*, 2019, **48**, 17874–17886.

30 T. Coradin, O. Durupthy and J. Livage, Interactions of amino-containing peptides with sodium silicate and colloidal silica: a biomimetic approach of silicification, *Langmuir*, 2002, **18**, 2331–2336.

31 S. Ahoulou, N. Vila, S. Pillet, D. Schaniel and A. Walcarius, Coordination polymers as template for mesoporous silica films: a novel composite material $Fe(Htrz)_3@SiO_2$ with remarkable electrochemical properties, *Chem. Mater.*, 2019, **31**(15), 5796–5087.

32 Q. Y. Hu, X. W. Liu, L. Tang, D. W. Min, T. C. Shi and W. Zhang, Pd–ZnO nanowire arrays as recyclable catalysts for 4-nitrophenol reduction and Suzuki coupling reactions, *RSC Adv.*, 2017, **7**, 7964–7972.

33 X. M. Gu, W. Qi, X. Z. Xu, Z. H. Sun, L. Y. Zhang, W. Liu, X. L. Pan and D. S. Su, Covalently functionalized carbon nanotube supported Pd nanoparticles for catalytic reduction of 4-nitrophenol, *Nanoscale*, 2014, **6**, 6609–6616.

34 C. H. Liu, R. H. Liu, Q. J. Sun, J. B. Chang, X. Gao, Y. Liu, S. T. Lee, Z. H. Kang and S. D. Wang, Controlled synthesis and synergistic effects of graphene-supported PdAu bimetallic nanoparticles with tunable catalytic properties, *Nanoscale*, 2015, **7**, 6356–6362.

35 C. H. Liu, J. Liu, Y. Y. Zhou, X. L. Cai, Y. Lu, X. Gao and S. D. Wang, Small and uniform Pd monometallic/bimetallic nanoparticles decorated on multi-walled carbon nanotubes for efficient reduction of 4-nitrophenol, *Carbon*, 2015, **94**, 295–300.

36 A. Chandra and M. Singh, Biosynthesis of amino acid functionalized silver nanoparticles for potential catalytic and oxygen sensing applications, *Inorg. Chem. Front.*, 2018, **5**, 233–257.

37 P. Zhang, C. Shao, X. Li, M. Zhang, X. Zhang, C. Su, N. Lu, K. Wang and Y. Liu, An electron-rich free-standing carbon@Au core–shell nanofiber network as a highly active and recyclable catalyst for the reduction of 4-nitrophenol, *Phys. Chem. Chem. Phys*, 2013, **15**, 10453–10458.